

Secular craton evolution due to cyclic deformation of underlying dense mantle lithosphere

Received: 8 April 2022

Yaoyi Wang  ^{1,4}, Zebin Cao  ^{1,4}, Lihang Peng  ¹, Lijun Liu  ^{1,2}✉, Ling Chen  ², Craig Lundstrom  ¹, Diandian Peng ¹ & Xiaotao Yang  ³

Accepted: 15 May 2023

Published online: 12 June 2023

 Check for updates

The cratonic crust is the most long-lived tectonic unit on Earth. The longevity of Earth's cratonic crust has been attributed to neutrally buoyant and mechanically strong lithospheric keels. However, this is inconsistent with observed secular cratonic deformation and alteration. Here we analyse the density profile and dynamic evolution of the lithospheric mantle underlying cratons to show that cratonic lithosphere may have experienced continuous and cyclic deformation and evolution since the break-up of the Rodinia supercontinent ~800 million years ago. We find that the thickness of cratonic crust correlates linearly with that of the mantle lithosphere, suggesting coupled evolution. Seismic evidence for depth-dependent radial anisotropy implies that the dense lower cratonic lithosphere experienced pervasive vertical deformation consistent with delamination. Geologic data and azimuthal anisotropy further suggest repeated post-Rodinia thinning of cratonic lithosphere followed by gradual restabilization of the perturbed lower lithosphere. Geodynamic simulations support our interpretation that partial lithospheric delamination, potentially triggered by plume underplating, can generate rapid surface uplift and erosion, with subsequent lithospheric stabilization leading to gradual craton subsidence. We propose that Earth's long-lived cratons have been maintained by this cyclic deformation style since the Neoproterozoic.

Cratons, the oldest continental crusts, are thought to be underlain by thick melt-depleted lithospheric keels^{1–3}. Although the longevity of cratons is generally attributed to these viscously strong and compositionally buoyant keels^{1,2}, considerable variations in surface topography⁴ (by 2 km), crustal thickness⁵ (by 13 km) and lithosphere–asthenosphere boundary (LAB) depth⁶ (by 200 km) exist among different cratons (Fig. 1 and Extended Data Fig. 1). These variations in craton properties testify to observed secular alteration of cratonic lithospheres after their formation^{3,4,7,8}. Consequently, a fundamental question arises: why have most cratonic crusts remained structurally stable while

their underlying mantle lithospheres suffered prominent temporal changes? To understand this peculiar behaviour of craton evolution, we performed a multidisciplinary analysis of the density profile and dynamic evolution of the sub-cratonic lithospheric mantle (SCLM) using plate reconstruction, thermochronology, seismic images and geodynamic simulations.

Depth distribution of SCLM density

The density profile of the SCLM strongly influences the topography, evolution and crustal properties of cratons. The observed >10 km

¹Department of Earth Science and Environmental Change, University of Illinois at Urbana-Champaign, Urbana, IL, USA. ²State Key Laboratory of Lithospheric Evolution, Institute of Geology and Geophysics, Chinese Academy of Sciences, Beijing, China. ³Department of Earth, Atmospheric, and Planetary Sciences, Purdue University, West Lafayette, IN, USA. ⁴These authors contributed equally: Yaoyi Wang, Zebin Cao. ✉e-mail: ljliu@illinois.edu

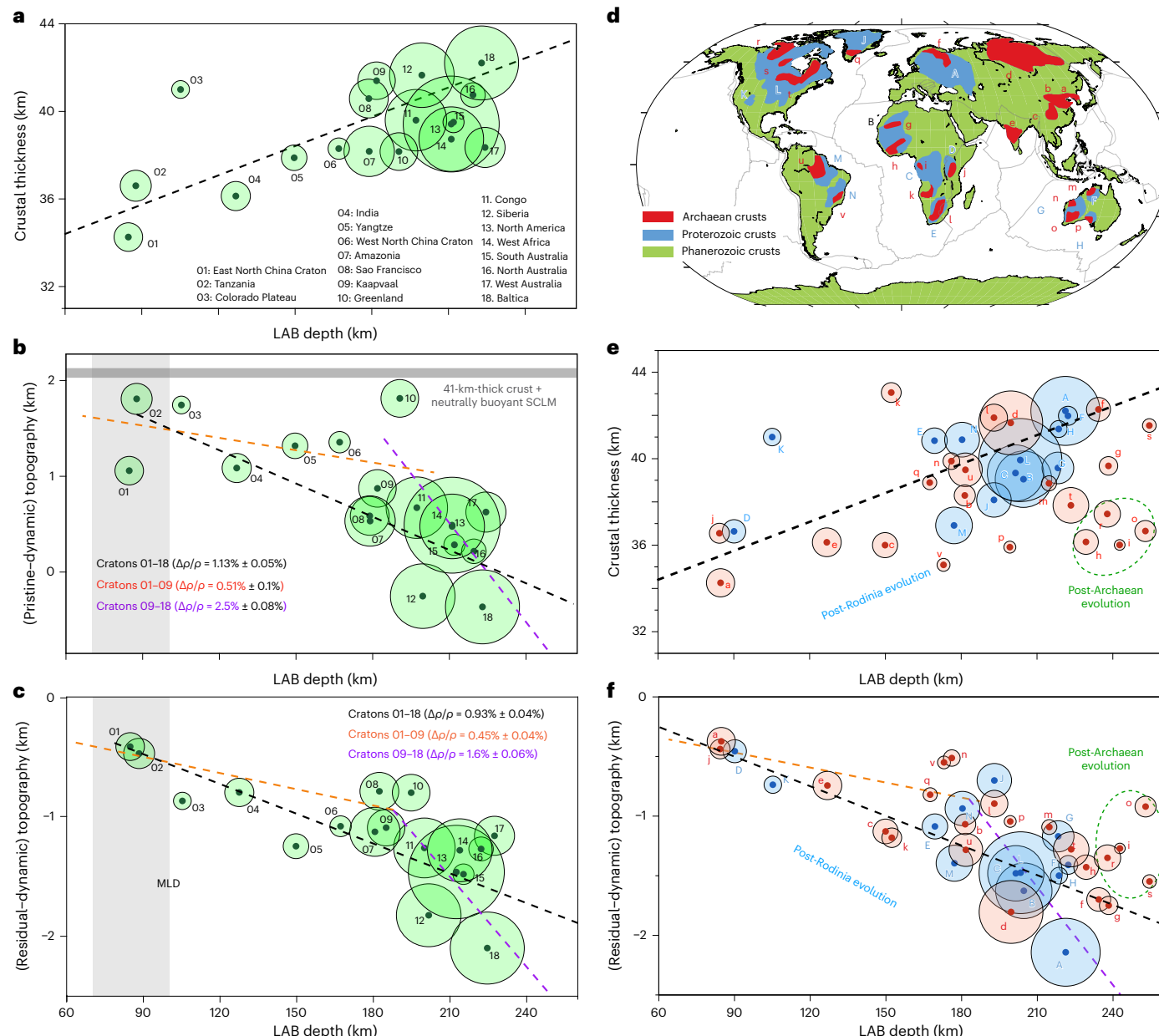


Fig. 1 | Relationship among craton topography, crustal thickness and LAB depth. **a**, Cratonic crustal thickness⁵ (sediment removed) versus LAB depth⁶. The dashed black line is an area-weighted linear fit to all craton data. The dark green dots mark the average values for each craton, with the corresponding standard deviations shown in Extended Data Fig. 2. The areas of the light green circles are proportional to the craton areas. Numbers 01–18 represent major cratons in Extended Data Fig. 1A. **b**, Pristine craton topography (with dynamic topography removed) versus LAB depth. The horizontal grey line shows the isostatic topography (relative to the -2.5 km average topography of mid-ocean ridges) for a craton with neutrally buoyant SCLM and 41-km-thick crust. The light grey column shows the depth range of the MLD. **c**, Residual craton topography

(relative to mid-ocean ridges, with dynamic topography removed) versus LAB depth. In **b**, **c**, the coloured dashed lines represent area-weighted linear fits among different numbers of cratons and corresponding density anomalies. **d**, Age of cratonic crusts (based on refs. 8,9), with Archaean and Proterozoic cratons labelled with lower- and upper-case letters, respectively. **e**, **f** Same relationships as in **a** and **c**, but for cratonic crusts with separate Archaean (red) and Proterozoic (blue) ages. The best-fitting trends remain the same as in **a** and **c**. The similar trends among most cratons imply they have a similar post-Rodinia evolution. The green dashed oval outlines a few small Archaean cratons that fall off these trends, probably reflecting a longer (post-Archaean) deformation history.

crustal thickness variation⁵ (Fig. 1a) reflects mostly thinner crust of small cratons relative to large ones. This observation dismisses a thinning mechanism due to lateral extension of an initially uniform crust since the corresponding average $\sim 30\%$ strain violates the definition of cratons, and this mechanism implies preferentially thin crusts within enlarged cratons, opposite to observed. Instead, the exposed Precambrian basement rocks, many representing exhumed middle to lower crust^{3,8,9}, occur predominantly in areas of thin crusts (Extended Data

Fig. 1b). This favours vertical tectonics where surface erosion represents the main mechanism of crustal thinning.

Interestingly, almost all cratons demonstrate a nearly linear dependence of crustal thickness on their LAB depth (Fig. 1a). The only exception is the Colorado Plateau, which seems to have experienced contradictory crustal shortening and lithospheric thinning during the Laramide Orogeny (mostly horizontal tectonics)¹⁰. This primary relationship implies a coupled evolutionary history between the crust

and SCLM, in contrast to the implied independent evolution of these two lithospheric layers from the isopycnicity hypothesis¹. The strong correlation between uplift and erosion^{4,7} suggests that long-term thinning of the SCLM caused surface uplift and crustal exhumation. This inference further favours the proposal of a denser-than-ambient SCLM¹¹ over the isopycnicity hypothesis¹ in that lithospheric thinning can cause notable surface uplift.

The depth profile of SCLM density may be derived from the principle of isostasy. Isolating the topographic contribution of the SCLM requires removal of the crustal effect. We approach this via two calculations: pristine topography and residual topography. The former estimates the topography with identical original crust for all cratons, while the latter removes the crustal effects on topography. More details of these two calculations are presented in Methods.

The resulting pristine craton topography is much lower (by up to 2 km) (Fig. 1b) than the isostatic topography of the pristine crust (grey line in Fig. 1b), suggesting that the SCLM must be denser than the ambient asthenosphere. We estimate this SCLM density profile by measuring the differential topography among cratons, where the amount of SCLM density anomaly follows $\Delta\rho/\rho_{\text{asthenosphere}} = \Delta(\text{topography})/\Delta(\text{LAB depth})$. Since most cratons' SCLM is thicker than 100 km (Fig. 1) where an intermittent mid-lithospheric discontinuity (MLD; ranging from 70 to 100 km depth) is commonly detected below cratons^{12,13}, a mean excess density of -1% for the sub-MLD lithosphere can be estimated (black dashed line in Fig. 1b). A closer examination of the data reveals a prominent change in the slope (-10×) of the topography versus LAB plot at ~190 km (coloured dashed lines in Fig. 1b), implying a dramatic increase in SCLM density (from <0.5% to 3%) below this depth.

The second calculation attempts to remove the topographic effects of craton crusts. After further removing dynamic topography (Extended Data Fig. 1d) from this residual topography, we arrive at another estimate of the SCLM's topographic effect (Fig. 1c). The overall negative (residual-dynamic) topography of as much as -2.5 km (Fig. 1c) confirms the higher-than-ambient density of SCLM. The associated topography-LAB depth trends are very close to those in the first approach but display considerably less scatter, especially for LAB shallower than 200 km, suggesting that the adopted crustal model CRUST1.0 (ref. 5) better captures the lateral crustal density variations neglected in the calculation of pristine topography (Fig. 1b).

Both the large mean density of the sub-MLD lithosphere and that of an even denser basal layer require that the net compositional density anomaly of the thick SCLM should be negligible to positive. We propose that the excess compositional density (relative to isopycnicity) represents an enrichment in mafic compositions such as garnet-lherzolite or eclogite. Such mafic enrichment within the SCLM can find extensive supports from xenolith data^{3,8,14,15}, high seismic velocities in the lower SCLM^{16,17} and inversions from topography, gravity and geoid^{11,18}. Tectonically, this dense component may reflect either ancient oceanic crust preserved from initial craton formation⁸ or subsequent refertilization¹⁴. Such a layered density structure also coincides with the transition from horizontally polarized fast seismic anisotropy orientation above the MLD to fast vertical polarization below the MLD^{19,20}, revealing contrasting deformation histories (Fig. 2 and Extended Data Fig. 3). These observations imply that the lower SCLM is gravitationally unstable and has experienced more vertical deformation than the upper portion.

Post-Rodinia cratonic lithosphere deformation

The layered density and anisotropy profiles of the cratonic lithosphere (Figs. 1 and 2) provide an intuitive solution to the observed SCLM deformation^{3,4,7,8}. By further considering the role of the MLD (Fig. 2), commonly considered a rheologically weak feature^{4,13,15}, we suggest the following two aspects of craton evolution. (1) The dense lower lithosphere is prone to delaminate along the spatially intermittent MLD in the presence of dynamic perturbations, while the buoyant and stiff upper lithosphere remains stable and protects the cratonic

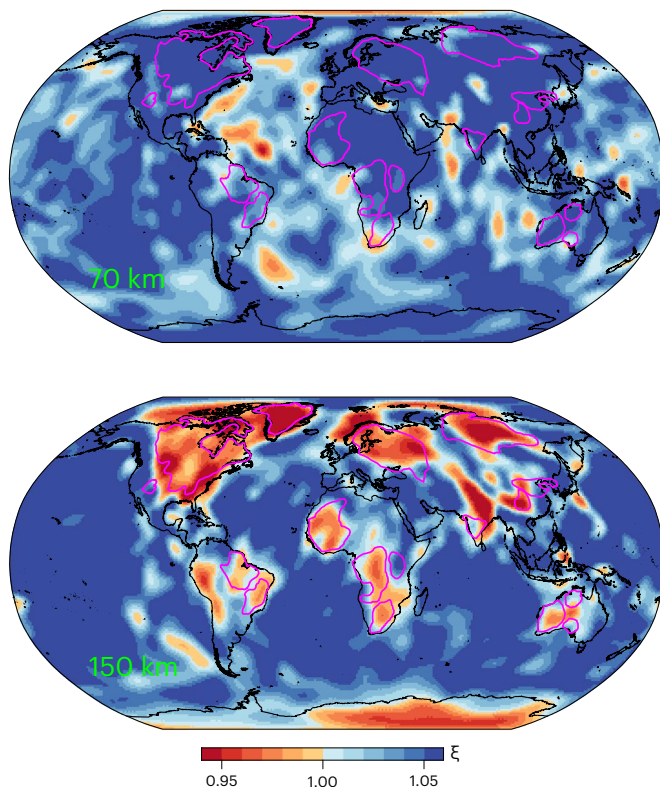


Fig. 2 | Globally observed lithospheric radial anisotropy above and below the MLD. V_{SH} and V_{SV} represent horizontal and vertical polarizations, respectively. $\xi = V_{\text{SH}}/V_{\text{SV}}$, and its values of >1 represent faster horizontal than vertical polarization. Magenta contours outline major cratons. Data from ref. 19.

crust from underlying perturbations. This delamination leads to lithospheric thinning, warming, surface uplift and crustal erosion, as illustrated from geologic records over supercontinent cycles (Figs. 1 and 3). (2) Most of the delaminated or detached lower lithosphere could relaminate after warming and/or losing some dense composition in the convective mantle, a process that restores lithospheric mass, allows the warmed lithosphere to cool and primes the lower SCLM for future instabilities. This long-term SCLM deformation with overall mass conservation could be recorded as depth-dependent radial and azimuthal anisotropy within the thick mantle lithosphere (Figs. 2 and 4). In the following, we substantiate these two aspects of SCLM evolution with more details.

First, to place some temporal constraints on the inferred coupled crust-SCLM evolution below cratons implied in Fig. 1a, we further examine the crustal thickness-LAB depth correlation against crustal ages (Fig. 1d). The first-order trends observed in the preceding analysis (Fig. 1a–c) remain for both Proterozoic and Archaean cratons: both age groups reveal a similar positive dependence of crustal thickness on LAB depth (Fig. 1e) and a similar negative relationship between (residual-dynamic) topography and LAB depth (Fig. 1f).

Given the dramatically longer duration of craton existence than that required for surface processes and internal dynamics to change lithospheric structures, the similar trends among these two age groups imply that most of the structural changes observed today should have occurred after the birth of the young cratons, many of which formed or stabilized as late as 1.2 billion years ago (Ga) (refs. 3,8,15). In addition, the sparsity of active tectonic events^{21–23} during the Proterozoic era (2.0–0.8 Ga) and the sluggish Precambrian continental motions²⁴ further imply that this geological period could have left a much weaker signature in the configuration of the present-day cratonic lithosphere than those from the Neoproterozoic–Phanerozoic period.

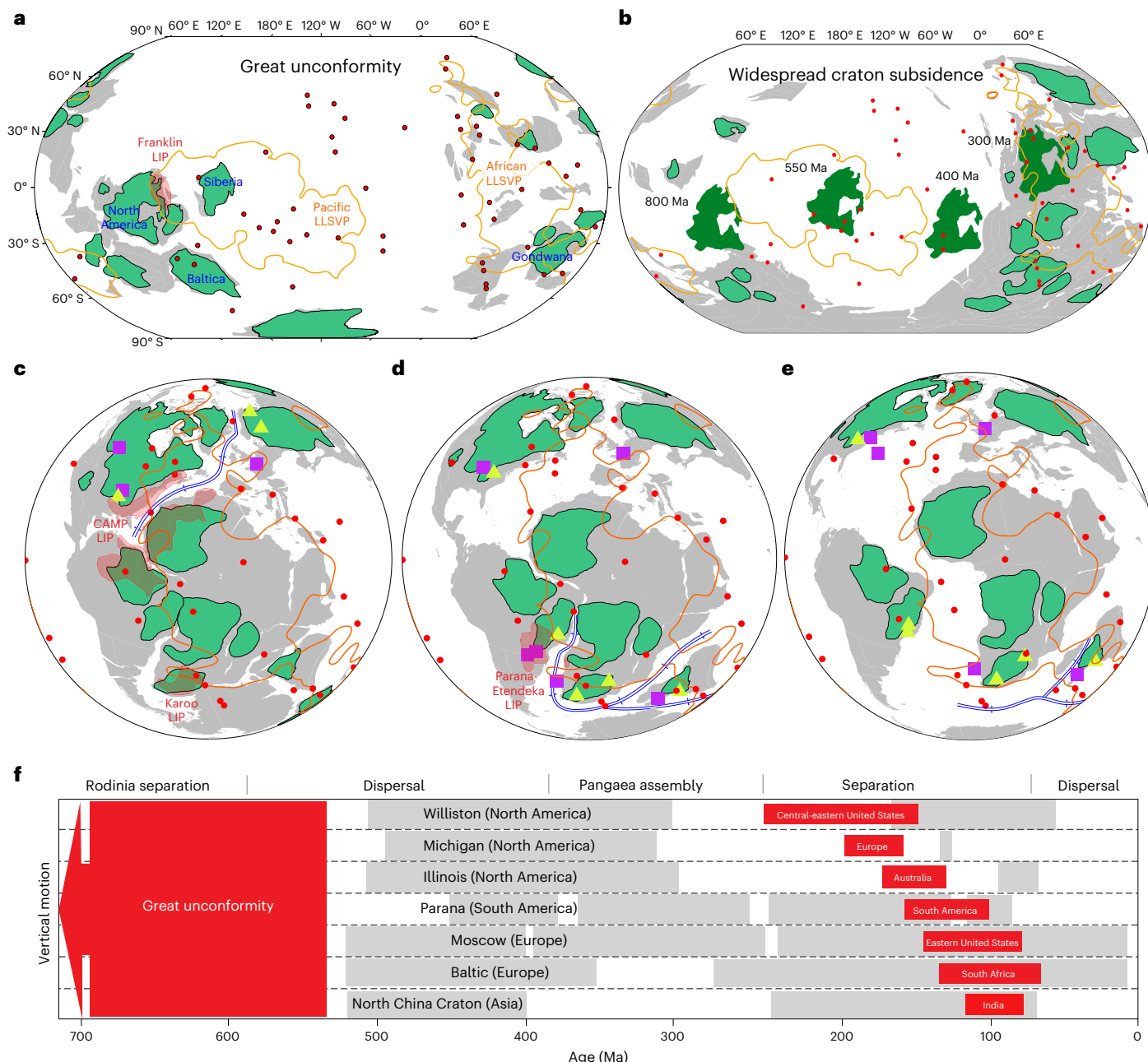


Fig. 3 | Craton locations relative to the deep mantle correlate with their vertical motion history. **a–e**, Reconstructed locations of cratons (light green areas)²⁹ at 720 Ma (**a**), 300 Ma (**b**), 180 Ma (**c**), 120 Ma (**d**) and 80 Ma (**e**). Dark green areas in **b** show the trajectory of North American craton from 800 to 300 Ma. Grey areas represent non-craton continents. Red dots represent hotspots²⁷ whose locations are assumed stationary. Red shaded areas mark major large igneous provinces (LIPs)²⁸. Orange contours outline the two stationary LLVPs, defined as seismic velocity perturbations of -0.6% at the core–mantle

boundary according to tomography S4ORTS²⁵. The light green triangles denote the positions of major unroofing events, following **f**. Purple squares mark enhanced sedimentation along continental margins or inland depression (Extended Data Table 1). Double blue lines with diverging arrows mark initial rifting locations³¹. **f**, Major uplift (red) and subsidence (grey) events over cratons since Rodinia separation (Extended Data Table 1). More-detailed reconstructions of tectonic features in **a–f** are available in Supplementary Videos 1 and 2.

It is possible that observations in Fig. 1d–f suffer a preservation bias. Archaean cratons display a stronger scattering than Proterozoic cratons, probably reflecting a longer tectonic history of the former. Indeed, the outliers consist of a few small Archaean cratons (inside the green dashed circle in Fig. 1e,f) that deviate from the main trends by having thinner crust and higher residual topography. In practice, the abnormal properties of these Archaean cores could be explained by additional lithospheric deformation before Rodinia, resulting in more crustal thinning (Fig. 5).

Second, we examine the spatial–temporal records for potential craton delamination and associated surface geology. Since most cratons are away from active plate boundaries, the triggering mechanisms for lithospheric delamination may include upwelling plumes and tectonic forces associated with supercontinent separation^{4,7}. In practice, we compare the recorded basement uplift/exhumation data with craton locations relative to the two large low-shear-velocity provinces (LLVPs)²⁵, which have probably remained stationary throughout the Phanerozoic²⁶ and are generally considered the source region of hotspots and large

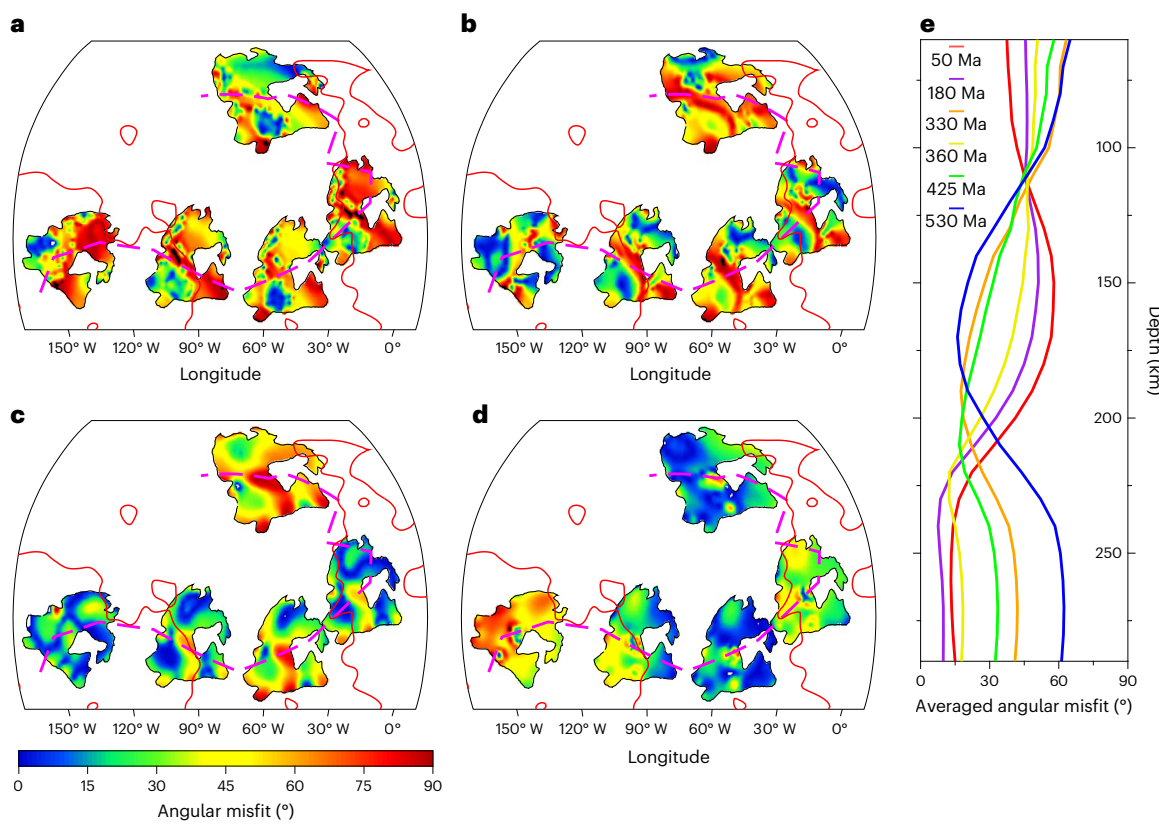


Fig. 4 | Comparison of reconstructed North American azimuthal anisotropy with Phanerozoic plate motion. **a–d**, Angular misfit (background color) between the averaged Phanerozoic North American plate motion and the reconstructed fast orientation of azimuthal anisotropy from YR2011³⁶ at 80 km (**a**), 130 km (**b**), 180 km (**c**) and 230 km (**d**) depths that are rotated back in time following past plate trajectory (the bold dashed magenta line) and rotation²⁹.

Each map corresponds to a different time interval (50 Myr for the Palaeozoic era and 100 Myr for the Mesozoic–Cenozoic eras) whose middle points are shown in **e**. Red contours outline the two LLSVPs. **e**, Spatially averaged angular misfit with respect to depth and time. A small misfit implies good alignment of lithospheric fabric with horizontal shearing at the corresponding depth and time. Note the anti-correlated misfit profiles between Palaeozoic and later.

igneous provinces^{26–28} (Fig. 3). This time frame coincides extensively with the last two supercontinent cycles (Rodinia and Pangaea)²⁹.

The Neoproterozoic break-up of Rodinia distributed most cratons near to/above the two LLSVPs and hotspots (Fig. 3a,b and Supplementary Video 1). The Neoproterozoic also marks the time of the Great Unconformity (GU), during which the cratons of North America, Siberia, Gondwana and Baltica (Fig. 3a) all experienced extensive surface exhumation³⁰. Among them, the greatest amount and extent of exhumation occurred in North America^{7,30,31} (Extended Data Table 1), where much of the upper crust of the Canadian Shield was removed, leading to a thin (35–38 km) crust today (Fig. 2b and Extended Data Fig. 1b). This could reflect the long duration (~500 Myr) that North America sat above the Pacific LLSVP (Fig. 3b and Supplementary Video 1). Similarly, other GU-bearing cratons also travelled above the LLSVPs around this time (Fig. 3a and Supplementary Video 1). This spatial–temporal correlation between craton location and uplift/exhumation (Fig. 3a,b) supports plume-driven delamination during supercontinent break-up. The subsequent movement of cratons away from the Pacific LLSVP during the Palaeozoic corresponds to global-scale craton subsidence and sedimentation³¹ (Fig. 3b,f), consistent with relamination (Fig. 5), cooling⁴ and/or refertilization³² of the SCLM that was disturbed in the Neoproterozoic. This situation persisted until Pangaea assembly by ~300 million years ago (Ma) when all landmasses finally aggregated above/near to the African LLSVP (Fig. 3b).

The Mesozoic separation of Pangaea starting at ~230 Ma (Fig. 3c–e and Supplementary Video 1) witnessed another phase of surface unroofing (Fig. 3f), during which cratons on both sides of the Atlantic Ocean migrated away from the African LLSVP while

traversing hotspots (Fig. 3c–f). Following the spatial migration of Atlantic opening (diverging blue lines in Fig. 3c–e), multiple uplift events occurred (Extended Data Table 1), first within central-eastern United States and western Baltica (Fig. 3c–f and Supplementary Video 2) and then along the southern Atlantic margin among Gondwana cratons (Fig. 3d). Meanwhile, the recorded exhumation history also correlates with the occurrence of large igneous provinces above the edge of LLSVPs (Fig. 3). During the subsequent Cenozoic dispersal of continents as they moved away from the LLSVP, craton exhumation largely stopped (Fig. 3f and Supplementary Video 2), consistent with the recovery of the Mesozoic lithospheric disturbance.

In theory, surface vertical motions could also originate from sub-lithospheric convection through dynamic topography^{33,34}. However, the observed cratonic exhumation, especially that formed the GU, straddled multiple continents³⁰ and could have lasted for hundreds of millions of years⁷ (Fig. 3f). Both these spatial and temporal scales are notably above those of dynamic topography^{33–35}. The same argument applies to the synchronized global onset of craton basins, which cannot be dynamically driven. More important, it is commonly perceived that mantle convection has limited impacts on the internal structures of the SCLM, a scenario opposite to observation (Figs. 1–4). Therefore, we propose that these uplift records (Fig. 3) should reflect contemporary SCLM delamination.

Cratonic lithosphere restoration after delamination

Depth-dependent lithospheric azimuthal anisotropy combined with past plate motions could reveal the temporal processes of SCLM

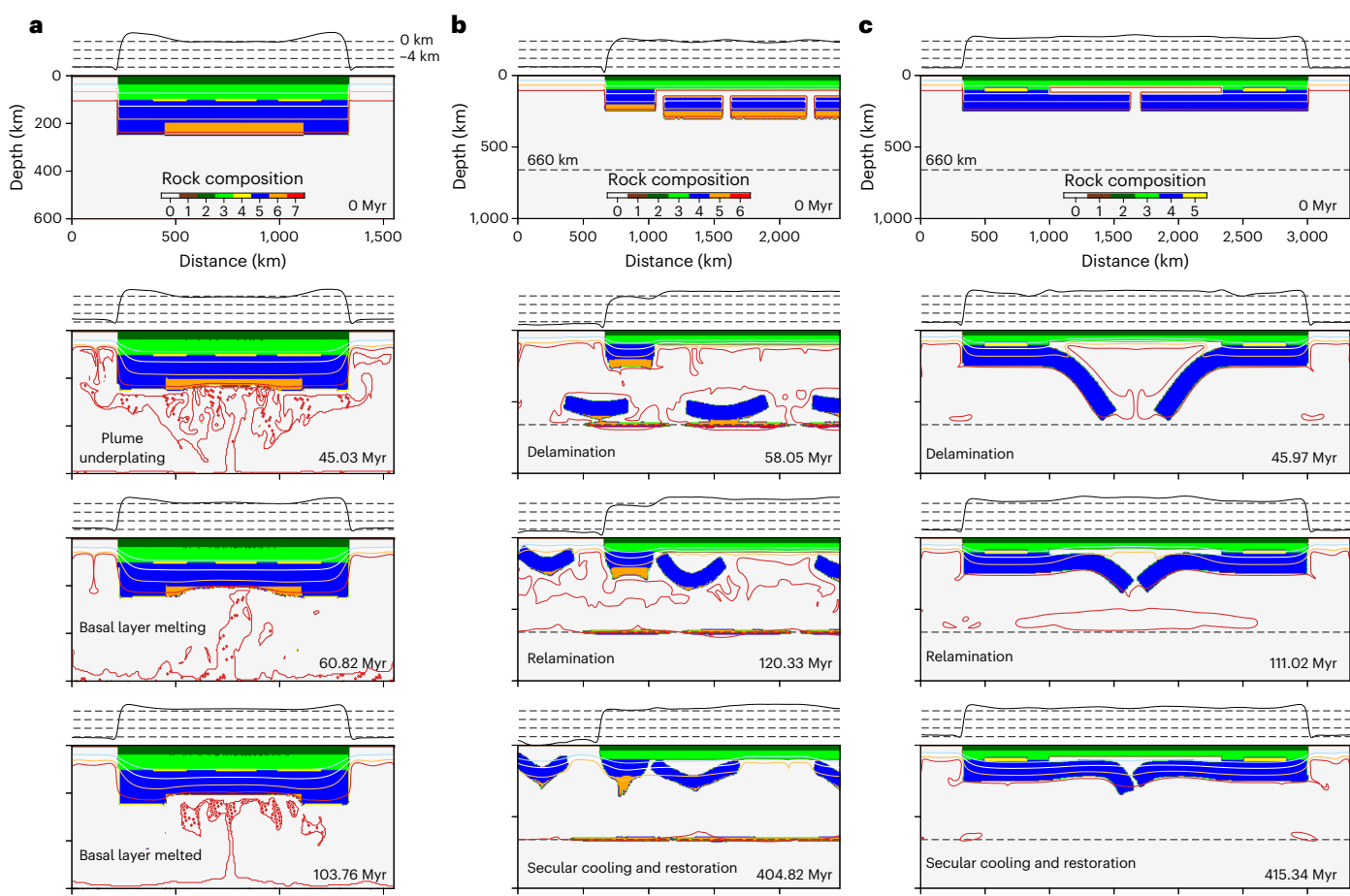


Fig. 5 | Three possible scenarios for the temporal evolution of SCLM. **a**, Model 1: a hot plume melts the basal mafic layer, causing surface uplift and lithospheric thinning. Background colours represent composition: 0, ambient mantle; 1, oceanic crust; 2, cratonic crust; 3, upper (<100 km) SCLM; 4, MLD; 5, lower SCLM with 0.3% excess density; 6, basal mafic layer with 3% excess density; 7, melt.

Overplotted are the evolving geotherms with a 200 °C increment. The top of each panel shows surface topography. **b**, Model 2: full delamination of lower SCLM segments. Compositions are the same as in **a** but without the MLD. **c**, Model 3: partial delamination of two SCLM segments.

restoration⁴. Due to both its intimate involvement in the relevant tectonics and high-quality data records (Figs. 1–3), North America, the largest craton, represents an ideal location for examining this tectonic–seismic relationship. We utilized a recent seismic model³⁶ that resolves anisotropy down to >300 km, covering the entire cratonic lithosphere. We calculated the angular misfit between the observed fast seismic splitting orientation at different depths and the absolute plate motion (APM) paths since the Rodinia breakup (Fig. 4).

Anisotropy within the uppermost (80 km) SCLM (Fig. 4a,e) correlates poorly (mean angular misfits of >50°) with all Palaeozoic APM paths and slightly better with the post-Pangaea (after 200 Ma) APM (misfits of ~40°). This supports a general lack of deformation within this lithospheric layer since the Neoproterozoic. Below 100 km, the match of observed fabric with Palaeozoic APM steadily improves while that with post-Pangaea APM decreases (Fig. 4e), with the former overpassing the latter at 110 km (Fig. 4b,e). This trend continues with increasing depth, where the smallest average misfit (as low as 15°) with Cambrian (530 Ma) APM occurs at ~170 km, and that with other subsequent Palaeozoic paths occurs continuously deeper until ~220 km, where the fabric best fits (~12°) with 360 Ma APM (Fig. 4c–e). Meanwhile, the misfit with post-Pangaea APM keeps increasing with depth to ~60° at 170 km (Fig. 4c,e), below which it starts to decrease to as low as 10° below 220 km. Within the lowest lithosphere (>200 km), where the post-Pangaea misfits have the lowest values, those for most Palaeozoic

paths notably increase with depth, with a general trend of larger misfits corresponding to earlier APM.

Another recent seismic model³⁷ reveals a similar correlation between the depth-dependent lithospheric azimuthal anisotropy and past APM of North America since 500 Ma (Extended Data Fig. 4). Mechanistically, the observed azimuthal anisotropy should record shearing between the restabilizing lithosphere and the asthenosphere after delamination⁴. This process probably lasts for hundreds of millions of years. The strong correlation between North American anisotropy at 100–200 km depth with the Palaeozoic APM reveals that the lower SCLM was restabilizing during this period, as this also explains the continent-wide subsidence and basin formation³¹ (Fig. 3). This requires the initial delamination (thus surface uplift) to have occurred in the Neoproterozoic, as is observationally supported by the enduring craton-plume (rising from the Pacific LLSVP) interaction²⁹ before 500 Ma (Fig. 3a,b) and the widespread GU-forming crustal exhumation^{7,30,31}. By contrast, the lowermost lithosphere fabric correlates well with post-Pangaea APM, indicating mild lithospheric perturbation near the base of the SCLM as North America cruised over the edge of the African LLSVP since 300 Ma (Fig. 3c–e), also consistent with localized surface uplifts during Pangaea separation (Fig. 3c–f).

The preceding analysis is further evidenced within other cratons during Pangaea separation⁴, where the lower (>100 km) lithosphere of these cratons could have delaminated during Pangaea separation, and the subsequent lithospheric recovery also reset its lithospheric

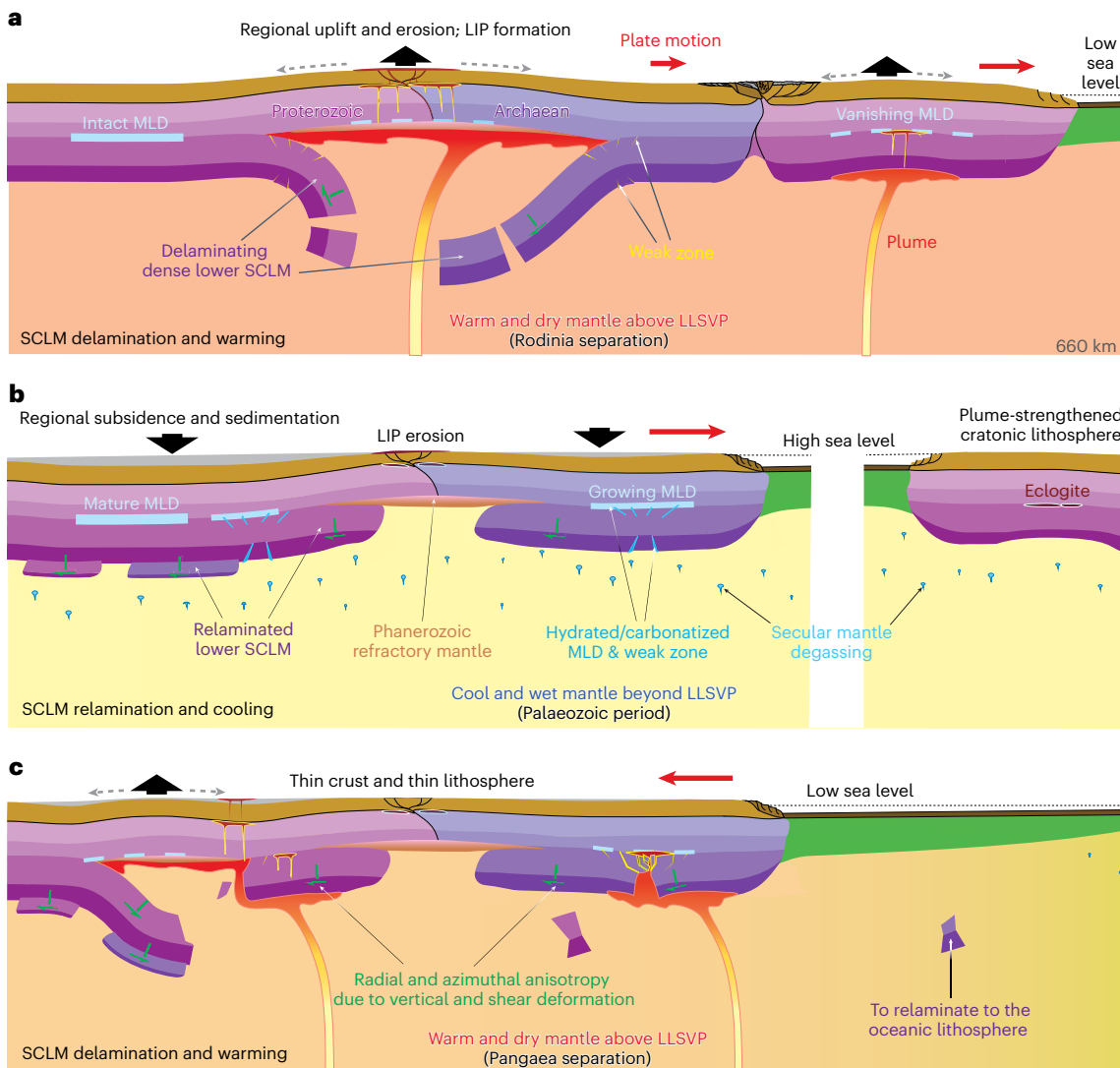


Fig. 6 | Cyclic deformation of the SCLM since the Neoproterozoic. The left continent acts as the reference frame. The envisaged evolution spans two successive supercontinent (**a,c**) and one inter-supercontinent (**b**) periods.

The illustration involves all scenarios of SCLM deformation shown in Fig. 5, and the resulting tectonic responses echo observations in Figs. 1–4. Both spatial variations (**a** versus **b;c**) and secular cooling (**a** versus **c**) of the ambient mantle are implied.

fabric. Collectively, the realignment of the lower lithosphere fabric below these cratons during the Phanerozoic (North America; Fig. 4) and Mesozoic–Cenozoic (Gondwana⁴), long after the time of craton formation, requires large-scale lithospheric deformation and restoration. Consequently, the anisotropy data support lower lithosphere restoration after delamination, during which the gradual downward resettlement (via re-lamination and cooling) of the disturbed lithosphere (Fig. 5) recorded both the vertical deformation (Fig. 2) and lateral shearing relative to the asthenosphere (Fig. 4) accompanying this process.

Geodynamic implications of cyclic SCLM deformation

As another sanity check, we develop numerical models to verify the possible geodynamic processes (Methods). The model set-up and parameters follow our recent studies^{38,39}. We consider three relevant scenarios (Models 1–3 in Fig. 5). Scenario one mimics an underplating hot plume that thins the dense basal layer whose melting point is lower than the rest of the lithosphere (see Methods for model details). In this model (Fig. 5a), the dense mafic basal layer gradually melts over the course of ~100 Myr, leading to moderate lithospheric thinning (by ~50 km) and surface uplift (~0.5 km).

Scenario two considers complete delamination of the lower SCLM (Fig. 5b), following our recent work³⁸. The dense lower lithosphere pieces descend to the base of the upper mantle after ~50 Myr. During this process, the delaminated lithosphere gradually warms and loses its negative thermal buoyancy. As the compositionally buoyant portion (blue colour in Fig. 5) starts to ascend, the dense basal layer detaches and ponds near 660 km depth (Fig. 5b). The re-laminated pieces gradually cool and freeze into the upper lithosphere, while the surface topography gradually lowers by >1 km to form intra-cratonic basins³⁸. The gradual restoration of the re-laminated lithosphere should be prone to form both radial and azimuthal anisotropy (Figs. 2 and 4).

Scenario three simulates partial delamination of the lower SCLM, where the spatially intermittent MLD and suture/weak zones determine the position of delamination (Fig. 5c). This is similar to that in Fig. 5b, except that only one end of the SCLM segments is initially decoupled. For simplicity, the dense basal layer is omitted. The evolution of this model is similar to scenario two except that all SCLM segments always restore close to their original locations. This model generates the most topographic variation (>2 km) among all scenarios.

We also performed two billion-year-duration simulations (Extended Data Figs. 5 and 6 and Supplementary Videos 3 and 4) with

different compositional layering. We observe multiple phases of delamination and relamination, reminiscent of the cyclic SCLM deformation discussed. The cyclic occurrence of elevated (~2 km) craton topography, each lasting 100–300 Myr, could have resulted in >10 km (via isostasy) of crustal erosion, consistent with observed crustal thinning (Fig. 1a) and exhumation during the GU⁷ (Fig. 3).

Collectively, our multidisciplinary analysis on the structural and dynamic properties of the SCLM (Figs. 1, 2, 4, 5) with cascading time constraints (Figs. 1d–f and 3–5) reveals that the cratonic lithosphere has probably been subject to cyclic deformation since Rodinia separation (Fig. 6). Key driving factors for this peculiar style of evolution include a denser-than-ambient SCLM, spatially and temporally varying MLD and lithospheric weak zones, as well as underlying mantle dynamics (Fig. 6). The location of cratons relative to the LLSVPs may determine whether the SCLM will suffer underplating of hot plumes or secular mantle dehydration⁴⁰, with the former leading to SCLM delamination⁴ or re-cratonicization⁴¹ depending on the pre-condition of the lithosphere, while the latter usually results in SCLM cooling and restoration, as well as MLD growth (Fig. 6). This repeated alteration of SCLM buoyancy may also contribute to the cyclic Phanerozoic global sea-level variations, with low stands during supercontinent periods and high stands during continental dispersals^{42,43} (Fig. 6).

The commencement of this dynamic history (Fig. 6) marks the end of the tectonically quiet Mesoproterozoic era, before which the hotter-than-present Archaean mantle⁴⁴ favours shallow to flat subduction of buoyant oceanic plates^{8,21}, allowing net accumulation of mafic materials within the SCLM during craton formation. Subsequent cooling of the ambient mantle⁴⁵ increases the negative buoyancy of the SCLM, as well as its gravitational instability. The debut of modern-style steep subduction during the Neoproterozoic^{23,24} could have hydrated the mantle since then⁴⁵, where hydrous melting during either Proterozoic craton formation or subsequent evolution could severely weaken the SCLM (along the MLD and sutures; Fig. 6), triggering the onset of continental-scale delamination (Fig. 5b,c and Extended Data Fig. 6) marked by the GU^{7,30}. In this case, the Neoproterozoic delamination event should be the most prominent in both spatial scale and extent of lithospheric perturbation, while the subsequent ones are probably secondary, consistent with the globally prominent Rodinia-affiliated craton exhumation and Palaeozoic subsidence (Fig. 3). We conclude that this cyclic deformation characterizes and maintains the longevity of cratons.

Online content

Any methods, additional references, Nature Portfolio reporting summaries, source data, extended data, supplementary information, acknowledgements, peer review information; details of author contributions and competing interests; and statements of data and code availability are available at <https://doi.org/10.1038/s41561-023-01203-5>.

References

- Jordan, T. H. Composition and development of the continental tectosphere. *Nature* **274**, 544–548 (1978).
- Lenardic, A. & Moresi, L. N. Some thoughts on the stability of cratonic lithosphere: effects of buoyancy and viscosity. *J. Geophys. Res.* **104**, 12747–12758 (1999).
- Carlson, R. W., Pearson, D. G. & James, D. E. Physical, chemical, and chronological characteristics of continental mantle. *Rev. Geophys.* **43**, RG1001 (2005).
- Hu, J. et al. Modification of the Western Gondwana craton by plume-lithosphere interaction. *Nat. Geosci.* **11**, 203–210 (2018).
- Laske, G., Masters, G., Ma, Z. & Pasyanos, M. Update on CRUST1.0-A 1-degree global model of Earth's crust. *Geophys. Res. Abstracts* **15**, abstr. EGU2013-2658 (2013).
- Schaeffer, A. J. & Lebedev, S. Global shear speed structure of the upper mantle and transition zone. *Geophys. J. Int.* **194**, 417–449 (2013).
- DeLucia, M. S., Guenthner, W. R., Marshak, S., Thomson, S. N. & Ault, A. K. Thermochronology links denudation of the Great Unconformity surface to the supercontinent cycle and snowball Earth. *Geology* **46**, 167–170 (2018).
- Lee, C.-T. A., Luffi, P. & Chin, E. J. Building and destroying continental mantle. *Annu. Rev. Earth Planet. Sci.* **39**, 59–90 (2011).
- Read, G. et al. Stratigraphic relations, kimberlite emplacement and lithospheric thermal evolution, Quiricó Basin, Minas Gerais State, Brazil. *Lithos* **77**, 803–818 (2004).
- Liu, L. et al. The role of oceanic plateau subduction in the Laramide orogeny. *Nat. Geosci.* **3**, 353–357 (2010).
- Wang, Y., Liu, L. & Zhou, Q. Topography and gravity reveal denser cratonic lithospheric mantle than previously thought. *Geophys. Res. Lett.* **49**, e2021GL096844 (2022).
- Fischer, K. M. et al. The lithosphere–asthenosphere boundary. *Annu. Rev. Earth Planet. Sci.* **38**, 551–575 (2010).
- Chen, L. Layering of subcontinental lithospheric mantle. *Sci. Bull.* **62**, 1030–1034 (2017).
- Griffin, W. L. et al. The origin and evolution of Archean lithospheric mantle. *Precambrian Res.* **127**, 19–41 (2003).
- Zhu, R., Zhao, G., Xiao, W., Chen, L. & Tang, Y. Origin, accretion, and reworking of continents. *Rev. Geophys.* **59**, e2019RG000689 (2021).
- Adams, A. & Nyblade, A. Shear wave velocity structure of the southern African upper mantle with implications for the uplift of southern Africa. *Geophys. J. Int.* **186**, 808–824 (2011).
- Garber, J. M. et al. Multidisciplinary constraints on the abundance of diamond and eclogite in the cratonic lithosphere. *Geochem. Geophys. Geosyst.* **19**, 2062–2086 (2018).
- Wang, Y., Liu, L. & Zhou, Q. Geoid reveals the density structure of cratonic lithosphere. *J. Geophys. Res.* **127**, e2022JB024270 (2022).
- Ho, T., Priestley, K. & Debayle, E. A global horizontal shear velocity model of the upper mantle from multimode Love wave measurements. *Geophys. J. Int.* **207**, 542–561 (2016).
- Porritt, R. W., Becker, T. W., Boschi, L. & Auer, L. Multiscale, radially anisotropic shear wave imaging of the mantle underneath the contiguous United States through joint inversion of USAArray and global data sets. *Geophys. J. Int.* **226**, 1730–1746 (2021).
- Pearson, D. G. & Wittig, N. Formation of Archean continental lithosphere and its diamonds: the root of the problem. *J. Geol. Soc.* **165**, 895–914 (2008).
- Tang, M., Chu, X., Hao, J. & Shen, B. Orogenic quiescence in Earth's middle age. *Science* **371**, 728–731 (2021).
- Stern, R. J. The Mesoproterozoic single-lid tectonic episode: prelude to modern plate tectonics. *GSA Today* <https://doi.org/10.1130/GSATG48OA.1> (2020).
- Bradley, D. C. Passive margins through Earth history. *Earth Sci. Rev.* **91**, 1–26 (2008).
- Ritsema, J., Deuss, A., Van Heijst, H. J. & Woodhouse, J. H. S4ORTS: a degree-40 shear-velocity model for the mantle from new Rayleigh wave dispersion, teleseismic traveltimes and normal-mode splitting function measurements. *Geophys. J. Int.* **184**, 1223–1236 (2011).
- Torsvik, T. H., Burke, K., Steinberger, B., Webb, S. J. & Ashwal, L. D. Diamonds sampled by plumes from the core–mantle boundary. *Nature* **466**, 352–355 (2010).
- King, S. D. & Adam, C. Hotspot swells revisited. *Phys. Earth Planet. Inter.* **235**, 66–83 (2014).
- Self, S., Schmidt, A. & Mather, T. A. in *Volcanism, Impacts, and Mass Extinctions: Causes and Effects* (eds Keller, G. & Kerr, A. C.) 319–337 (Geological Society of America, 2014).
- Merdith, A. S. et al. Extending full-plate tectonic models into deep time: linking the Neoproterozoic and the Phanerozoic. *Earth Sci. Rev.* **214**, 103477 (2020).

30. Peters, S. E. & Gaines, R. R. Formation of the ‘Great Unconformity’ as a trigger for the Cambrian explosion. *Nature* **484**, 363–366 (2012).
31. Allen, P. A. & Armitage, J. J. in *Tectonics of Sedimentary Basins: Recent Advances* (eds Busby, C. & Azor, A.) 602–620 (Wiley, 2012).
32. Liu, L. et al. Development of a dense cratonic keel prior to the destruction of the North China Craton: constraints from sedimentary records and numerical simulation. *J. Geophys. Res. Solid Earth* **124**, 13192–13206 (2019).
33. Gurnis, M., Mitravica, J. X., Ritsema, J. & van Heijst, H. J. Constraining mantle density structure using geological evidence of surface uplift rates: the case of the African Superplume. *Geochem. Geophys. Geosyst.* **1**, 1020 (2010).
34. Liu, L. The ups and downs of North America: evaluating the role of mantle dynamic topography since the Mesozoic. *Rev. Geophys.* **53**, 1022–1049 (2015).
35. Liu, L. & Gurnis, M. Dynamic subsidence and uplift of the Colorado Plateau. *Geology* **38**, 663–666 (2010).
36. Yuan, H. & Romanowicz, B. Lithospheric layering in the North American craton. *Nature* **466**, 1063–1068 (2010).
37. Schaeffer, A. J., Lebedev, S. & Becker, T. W. Azimuthal seismic anisotropy in the Earth’s upper mantle and the thickness of tectonic plates. *Geophys. J. Int.* **207**, 901–933 (2016).
38. Peng, L., Liu, L. & Liu, L. The fate of delaminated cratonic lithosphere. *Earth Planet. Sci. Lett.* **594**, 117740 (2022).
39. Hu, J., Liu, L. & Gurnis, M. Southward expanding plate coupling due to variation in sediment subduction as a cause of Andean growth. *Nat. Commun.* **12**, 7271 (2021).
40. Liu, J. et al. Plume-driven retronization of deep continental lithospheric mantle. *Nature* **592**, 732–736 (2021).
41. Fu, H.-Y., Li, Z.-H. & Chen, L. Continental mid-lithosphere discontinuity: a water collector during craton evolution. *Geophys. Res. Lett.* **49**, e2022GL101569 (2022).
42. Gurnis, M. Large-scale mantle convection and the aggregation and dispersal of supercontinents. *Nature* **322**, 695–699 (1988).
43. Hallam, A. *Phanerozoic Sea-Level* (Columbia Univ. Press, 1992).
44. Herzberg, C., Condie, K. & Korenaga, J. Thermal history of the Earth and its petrological expression. *Earth Planet. Sci. Lett.* **292**, 79–88 (2010).
45. Korenaga, J. Initiation and evolution of plate tectonics on Earth: theories and observations. *Annu. Rev. Earth Planet. Sci.* **41**, 117–151 (2013).

Publisher's note Springer Nature remains neutral with regard to jurisdictional claims in published maps and institutional affiliations.

Springer Nature or its licensor (e.g. a society or other partner) holds exclusive rights to this article under a publishing agreement with the author(s) or other rightsholder(s); author self-archiving of the accepted manuscript version of this article is solely governed by the terms of such publishing agreement and applicable law.

© The Author(s), under exclusive licence to Springer Nature Limited 2023

Methods

Density structure of the SCLM

For both pristine and residual topography calculation, we avoid analysing cratons within 300 km from convergent boundaries (Extended Data Fig. 1a) where flexural and dynamic topography may be important. Estimating SCLM density using absolute topography may suffer uncertain topographic contributions from the crust and the convective mantle¹¹. Here we introduce a new approach by measuring the differential topography among cratons, where the amount of SCLM density anomaly follows $\Delta\rho/\rho_{\text{asthenosphere}} = \Delta(\text{topography})/\Delta(\text{LAB depth})$.

Pristine topography. In the calculation of pristine topography, we project all cratons to a nominal pristine crust (with a uniform 41 km thickness) that has not experienced erosion since its formation. The corresponding pristine topography (Extended Data Fig. 2) is estimated by restoring the lost topography due to erosion on the basis of the crustal thickness difference from the pristine state (Extended Data Fig. 2a,b). Neglecting possible geographic differences in crustal density (see further discussion that follows), the resulting topography variation (Extended Data Fig. 2c) reflects mostly that due to buoyancy of the underlying mantle. By correcting this topographic difference, we define the pristine surface topography for cratons following equation:

$$t_{\text{pris}} = t_{\text{obs}} + \frac{H_{\text{crust}} - H_0}{\text{mantle}} \times (\rho_{\text{mantle}} - \rho_{\text{crust}})$$

where t_{pris} and t_{obs} are pristine and observed surface topography, respectively; H_{crust} is the observed crustal thickness from CRUST1.0 (ref. 5); H_0 is the reference pristine crust thickness, with a value of 41 km; and ρ_{mantle} and ρ_{crust} are mantle and crustal densities, with values of 3.3 g cm⁻³ and 2.8 g cm⁻³, respectively.

Residual topography

By comparison, the residual topography calculation attempts to remove the topographic effect of craton crusts. In practice, this is realized by calculating residual topography, defined as observed topography minus the crustal contribution¹¹. We approximate the density and thickness of craton crusts using CRUST1.0, which considers geographically variable crustal properties from both seismology and geology; for regions where more-detailed measurements are available, the regional results^{13,46,47} (North China, Yangtze and Colorado Plateau) are adopted.

Dynamic topography. Since the concept of dynamic topography still lacks a unanimous definition, we define it as the topographic contribution from the convective mantle beneath the lithosphere. We estimate the dynamic topography by solving for the instantaneous global mantle flow using the spherical finite-element code CitcomS⁴⁸. The mantle density structure is converted from a shear-wave tomography S4ORTS²⁵ using an empirical seismic-to-density conversion (Extended Data Fig. 5a) following ref. 49. The resulting density anomalies are further converted to effective temperature perturbations, whose dynamic properties are solved for in a thermal–mechanical model.

We assume an incompressible mantle that satisfies the Boussinesq approximation. The two governing equations for the instantaneous convection are:

$$\nabla \cdot \vec{u} = 0$$

where \vec{u} is the velocity vector, P is dynamic pressure, η is dynamic viscosity, ρ_m is the density of ambient mantle, α is the thermal expansion coefficient, ΔT is temperature anomaly and \vec{g} is gravitational acceleration.

The three-dimensional structure of the effective mantle viscosity is dependent both on depth (Extended Data Fig. 5b) and on temperature following the equation:

$$\eta = \eta_{\text{ref}} \eta_0 e^{\frac{E}{T+T_0} - \frac{E}{1+T_0}}$$

where η is dynamic viscosity; η_{ref} is reference viscosity (for which we take 10²¹ Pa s in the calculation); η_0 is the viscosity prefactor, which is shown in Extended Data Fig. 5b; E is activation energy; T is non-dimensional temperature; and T_0 is non-dimensional ambient mantle temperature.

The convective mantle is defined as that below the LAB, estimated as the base of the high shear-wave heterogeneity (Extended Data Fig. 5), whose pattern and depth are similar to those in the LITHO1.0 model (Extended Data Fig. 1e)⁵⁰. In practice, we take 300 km as the LAB depth below continents and 200 km below oceans for the dynamic topography model (Fig. 2c), similar to previous studies^{11,51}. The surface dynamic topography is obtained from the sub-lithospheric normal stress using the following equation:

$$h = \frac{\tau}{\Delta\rho g}$$

where h is the surface dynamic topography, $\Delta\rho$ is the density contrast between mantle and water in oceans and that between mantle and air on continents; τ is the normal stress at surface; and g is gravitational acceleration.

We also perform more cases with different choices of model parameters (Extended Data Table 2) to test the robustness of the topography and gravity results (Extended Data Fig. 6) contributed from the convecting mantle.

Geodynamic modelling

General model set-up. We develop two-dimensional numerical models using the finite-element code CitcomS⁴⁸ to investigate the fate of delaminated cratonic lower lithosphere. These models solve thermal–chemical convection with temperature, composition and strain-rate-dependent rheology following our recent work^{38,39}. We assume an incompressible mantle with internal heating (Extended Data Table 2) that leads to ±100 °C temperature change over ~1 billion years, where the cooling is due to a greater heat loss at the surface than heat gain from the interior. We use tracers to define different model compositions (Extended Data Fig. 5a,d and Fig. 5). The SCLM tracers also carry compositional density anomalies of up to ~100 kg m⁻³ and an intrinsic viscosity up to three orders of magnitude larger than the ambient asthenosphere. The models incorporate depth-, temperature-, composition- and strain-rate-dependent rheology³⁸ (Extended Data Fig. 5). The resulting density and viscosity structures due to temperature and composition combined are shown in Extended Data Fig. 5. The strain-rate weakening further decreases the upper-mantle viscosity, thus increasing the total viscosity contrast to greater than six orders of magnitude (Extended Data Fig. 6), similar to our recent geophysical inversion⁵². The resulting upper-SCLM viscosity is large enough for the cratonic crust to remain stable during ~10⁹ years of evolution². Other model parameters with their physical values are listed in Extended Data Table 2.

Initial conditions of the numerical simulations. Here we present five different models. Model 1 (Fig. 5a) has an initially layered SCLM density structure, including a neutrally buoyant upper SCLM (green) and a denser-than-ambient (by 1.2%) lower SCLM, which further consists of a 90-km-thick upper layer (blue) that is compositionally buoyant (~26.6 kg m⁻³) and a 50-km-thick lower layer (brown) that is compositionally dense (90.6 kg m⁻³). A plume with a potential temperature of 1,550 °C and a radius of 50 km is initiated at the base of the upper mantle. The basal layer is considered as wet basalt–peridotite whose

melting curves are based on ref. 53. Model 2 (Fig. 5b) assumes delamination already happened at the initial time and some SCLM pieces are completely decoupled, following our recent study³⁸. These segments are separated from the surrounding SCLM by the material of the ambient asthenosphere. After sinking to the base of the upper mantle, the garnet–peridotite composition within the brown basal layer becomes more buoyant than the ambient mantle at 660–750 km depth range⁵⁴. Model 3 has the same set-up as Model 2, except that (1) the initial delaminated segments are decoupled at one end with the other end remaining intact, and (2) the dense basal layer is removed. Model 4 is the same as Model 2 but with a longer simulation period (>1 Gyr). Model 5 is similar to Model 4 but with a major difference being that the dense garnet–peridotite material follows a tilted stacking configuration within the lower SCLM. Detailed density and viscosity settings as represented by Models 4 and 5 are shown in Extended Data Fig. 5b,c.

Possible scenarios of SCLM deformation

We emphasize that the presented three geodynamic scenarios in the main text (Fig. 5) should be considered endmember cases. The reality could involve multiple dynamic scenarios (Fig. 6). For example, plume–lithosphere interaction is considered to both destroy⁴ and strengthen⁴⁰ the cratonic lithosphere. However, direct plume impacts on Phanerozoic SCLM evolution should be minor, given the small number of large igneous provinces since Rodinia separation (Fig. 3) that also occurred mostly along craton margins, in contrast to the widespread SCLM deformation (Figs. 2 and 4) and vertical movements with crustal thinning (Figs. 1 and 3). However, plume underplating could severely alter the volatile content of the lithosphere, especially the MLD and other weak zones whose mechanical strength may be dictated by the temporal behaviours of mantle degassing⁴¹, where the spatiotemporal variation of the MLD configuration could determine the long-term stability of the underlying SCLM (Fig. 6).

Data availability

The CRUST1.0 model is available at <https://igppweb.ucsd.edu/~gabi/crust1.html>. The LITHO1.0 model is available at <https://igppweb.ucsd.edu/~gabi/litho1.0.html>. The data for residual topography and residual gravity can be found at Zenodo (<https://doi.org/10.5281/zenodo.3940835>). The crustal age data are based on ‘World CGMW, 1:50 M, Geological Units Onshore’ with the permission of OneGeology at <http://portal.onegeology.org/OnegeologyGlobal/>. The seismic anisotropy data are available mostly from the original publications, and additional data can be found at <https://ds.iris.edu/ds/products/> and <https://schaeffer.ca/tomography/sl2016sva/>.

Code availability

The mantle convection code CitcomS is available at <https://geodynamics.org/cig/software/citcoms/>.

References

46. Zhang, Y., Chen, L., Ai, Y. & Jiang, M. Lithospheric structure beneath the central and western North China Craton and adjacent regions from S-receiver function imaging. *Geophys. J. Int.* **219**, 619–632 (2019).
47. Levander, A. & Miller, M. S. Evolutionary aspects of lithosphere discontinuity structure in the western US. *Geochem. Geophys. Geosyst.* **13**, Q0AK07 (2012).
48. Zhong, S., McNamara, A., Tan, E., Moresi, L. & Gurnis, M. A benchmark study on mantle convection in a 3-D spherical shell using CitcomS. *Geochem. Geophys. Geosyst.* **9**, Q10017 (2008).
49. Simmons, N. A., Forte, A. M. & Grand, S. P. Joint seismic, geodynamic and mineral physical constraints on three-dimensional mantle heterogeneity: implications for the relative importance of thermal versus compositional heterogeneity. *Geophys. J. Int.* **177**, 1284–1304 (2009).
50. Pasaynos, M., Masters, G., Laske, G., Laske, G. & Ma, Z. LITHO1.0: an updated crust and lithospheric model of the Earth. *J. Geophys. Res. Solid Earth* **119**, 2153–2173 (2014).
51. Liu, L., Spasojević, S. & Gurnis, M. Reconstructing Farallon plate subduction beneath North America back to the Late Cretaceous. *Science* **322**, 934–938 (2008).
52. Liu, L. & Hasterok, D. High-resolution lithosphere viscosity and dynamics revealed by magnetotelluric tomography. *Science* **353**, 1515–1519 (2016).
53. Gao, S., Takahashi, E. & Suzuki, T. High-pressure melting experiments on basalt–peridotite layered source (KLB-1/N-MORB): implications for magma genesis in Hawaii. *Int. J. Geosci.* <https://doi.org/10.4236/ijg.2017.81001> (2017).
54. Ballmer, M. D., Schmerr, N. C., Nakagawa, T. & Ritsema, J. Compositional mantle layering revealed by slab stagnation at ~1000-km depth. *Sci. Adv.* **1**, e1500815 (2015).
55. Poag, C. W. & Sevon, W. D. A record of Appalachian denudation in postrift Mesozoic and Cenozoic sedimentary deposits of the US Middle Atlantic continental margin. *Geomorphology* **2**, 119–157 (1989).
56. Guillocheau, F. et al. Quantification and causes of the terrigenous sediment budget at the scale of a continental margin: a new method applied to the Namibia–South Africa margin. *Basin Res.* **24**, 3–30 (2012).
57. Ault, A. K., Flowers, R. M. & Bowring, S. A. Phanerozoic surface history of the Slave craton. *Tectonics* **32**, 1066–1083 (2013).
58. Boettcher, S. S. & Milliken, K. L. Mesozoic–Cenozoic unroofing of the southern Appalachian Basin: apatite fission track evidence from middle Pennsylvanian sandstones. *J. Geol.* **102**, 655–663 (1994).
59. Boone, S. C., Seiler, C., Reid, A. J., Kohn, B. & Gleadow, A. An Upper Cretaceous paleo-aquifer system in the Eromanga Basin of the central Gawler Craton, South Australia: evidence from apatite fission track thermochronology. *Aust. J. Earth Sci.* **63**, 315–331 (2016).
60. Cederbom, C., Larson, S. Å., Tullborg, E. L. & Stiberg, J. P. Fission track thermochronology applied to Phanerozoic thermotectonic events in central and southern Sweden. *Tectonophysics* **316**, 153–167 (2000).
61. Fonseca, A. C. L. et al. Differential Phanerozoic evolution of cratonic and non-cratonic lithosphere from a thermochronological perspective: São Francisco Craton and marginal orogens (Brazil). *Gondwana Res.* **93**, 106–126 (2021).
62. Sahu, H. S., Raab, M. J., Kohn, B. P., Gleadow, A. J. W. & Bal, K. D. Thermal history of the Krishna–Godavari basin, India: constraints from apatite fission track thermochronology and organic maturity data. *J. Asian Earth Sci.* **73**, 1–20 (2013).
63. Stanley, J. R., Flowers, R. M. & Bell, D. R. Kimberlite (U–Th)/He dating links surface erosion with lithospheric heating, thinning, and metasomatism in the southern African Plateau. *Geology* **41**, 1243–1246 (2013).
64. Wildman, M. et al. Contrasting Mesozoic evolution across the boundary between on and off craton regions of the South African plateau inferred from apatite fission track and (U–Th–Sm)/He thermochronology. *J. Geophys. Res. Solid Earth* **122**, 1517–1547 (2017).

Acknowledgements

L.L. acknowledges partial support by NSF grant EAR2244660. L.C. acknowledges NSFC grant 42288201. We also acknowledge the use of Generic Mapping Tool (GMT) for plotting figures and the TACC supercomputing platform Frontera for carrying out the numerical simulations.

Author contributions

L.L. initiated and organized the project. Y.W. prepared the lithospheric and geological data. Z.C. analysed the seismic anisotropy. L.P. performed the numerical simulations. L.C. helped with seismology and tectonics. C.L. helped with petrology and tectonics. D.P. helped with modelling and graphics. X.Y. helped with seismic interpretation. L.L. wrote the paper with inputs from all authors.

Competing interests

The authors declare no competing interests.

Additional information

Extended data is available for this paper at
<https://doi.org/10.1038/s41561-023-01203-5>.

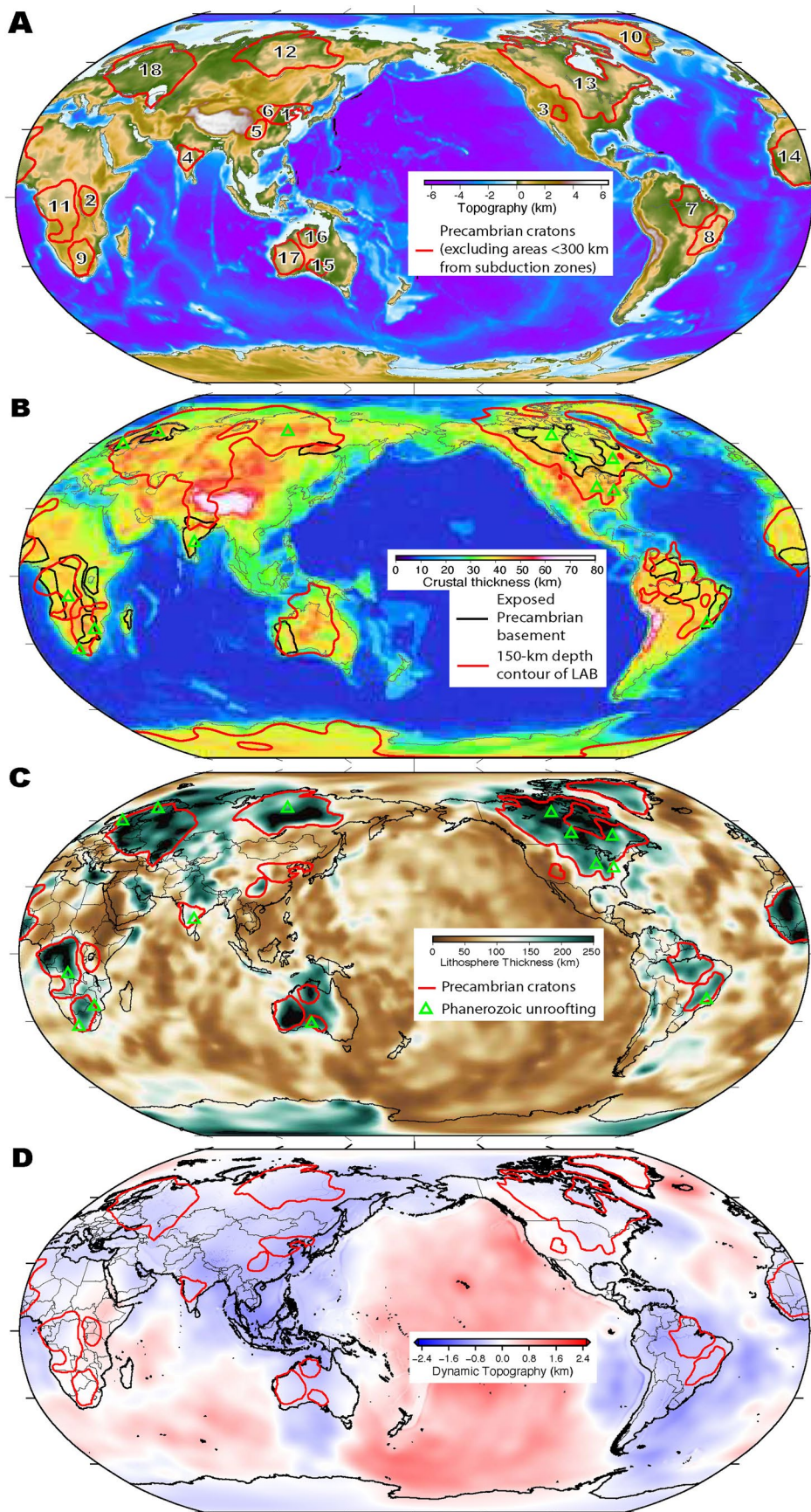
Supplementary information

The online version contains supplementary material available at
<https://doi.org/10.1038/s41561-023-01203-5>.

Correspondence and requests for materials should be addressed to Lijun Liu.

Peer review information *Nature Geoscience* thanks Hongliang Wang and the other, anonymous, reviewer(s) for their contribution to the peer review of this work. Primary Handling Editors: Louise Hawkins and Xujia Jiang, in collaboration with the *Nature Geoscience* team.

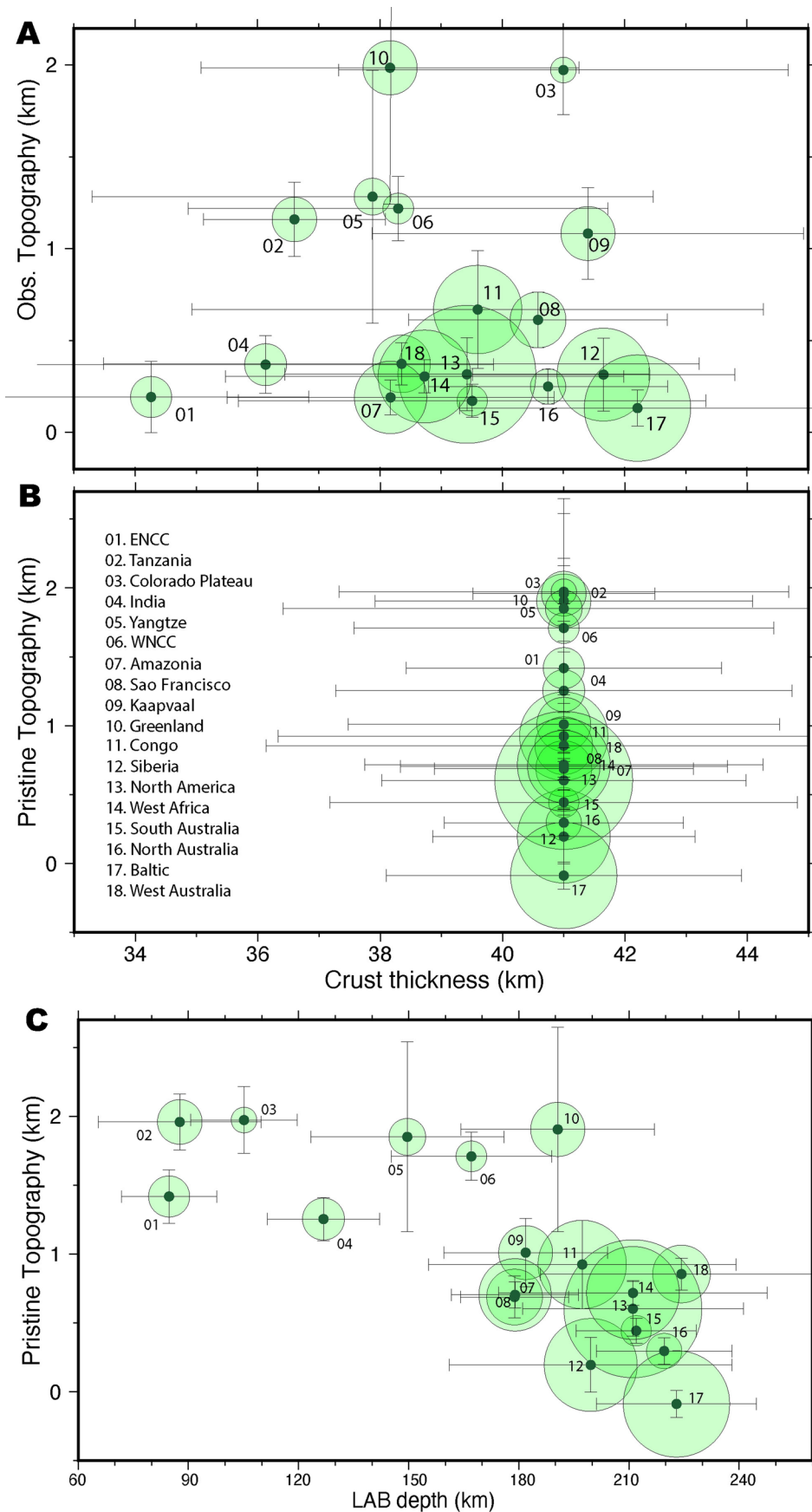
Reprints and permissions information is available at
www.nature.com/reprints.



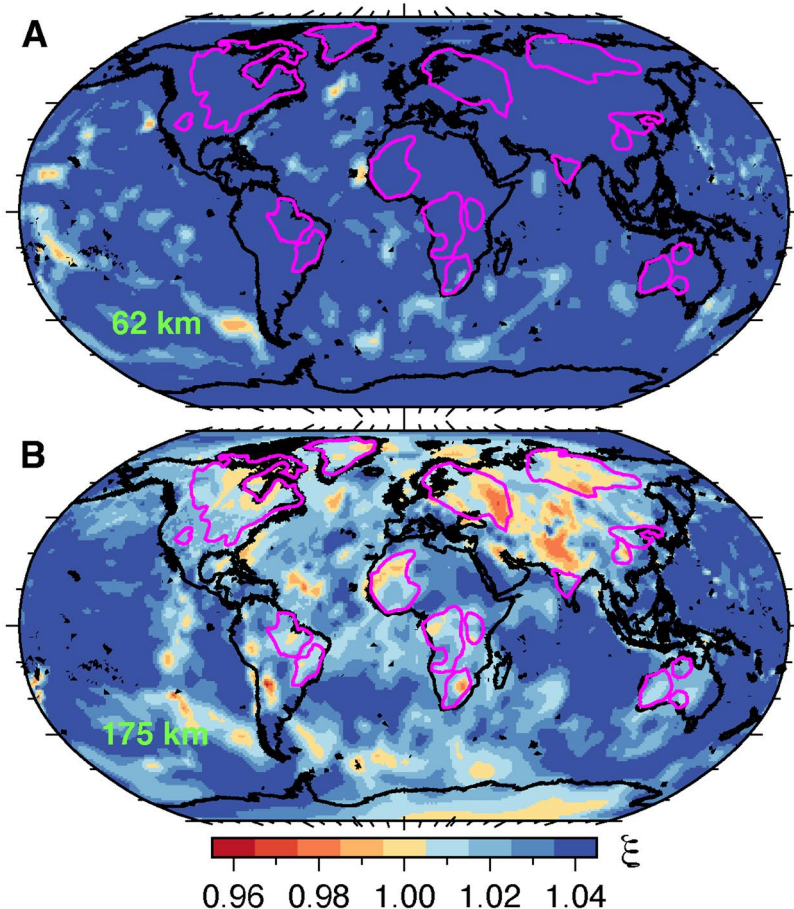
Extended Data Fig. 1 | See next page for caption.

Extended Data Fig. 1 | Surface topography and lithospheric structures of cratons. **(A)** Surface topography of major cratons (red contours, numbered from 1 to 18, all Precambrian crusts⁸). **(B)** Crustal thickness from CRUST1.0⁵. Red lines represent the 150-km depth contour for LAB⁶ in **C**. Black lines confine Archean–Neoproterozoic exposed basement rocks (based on OneGeology, See Data

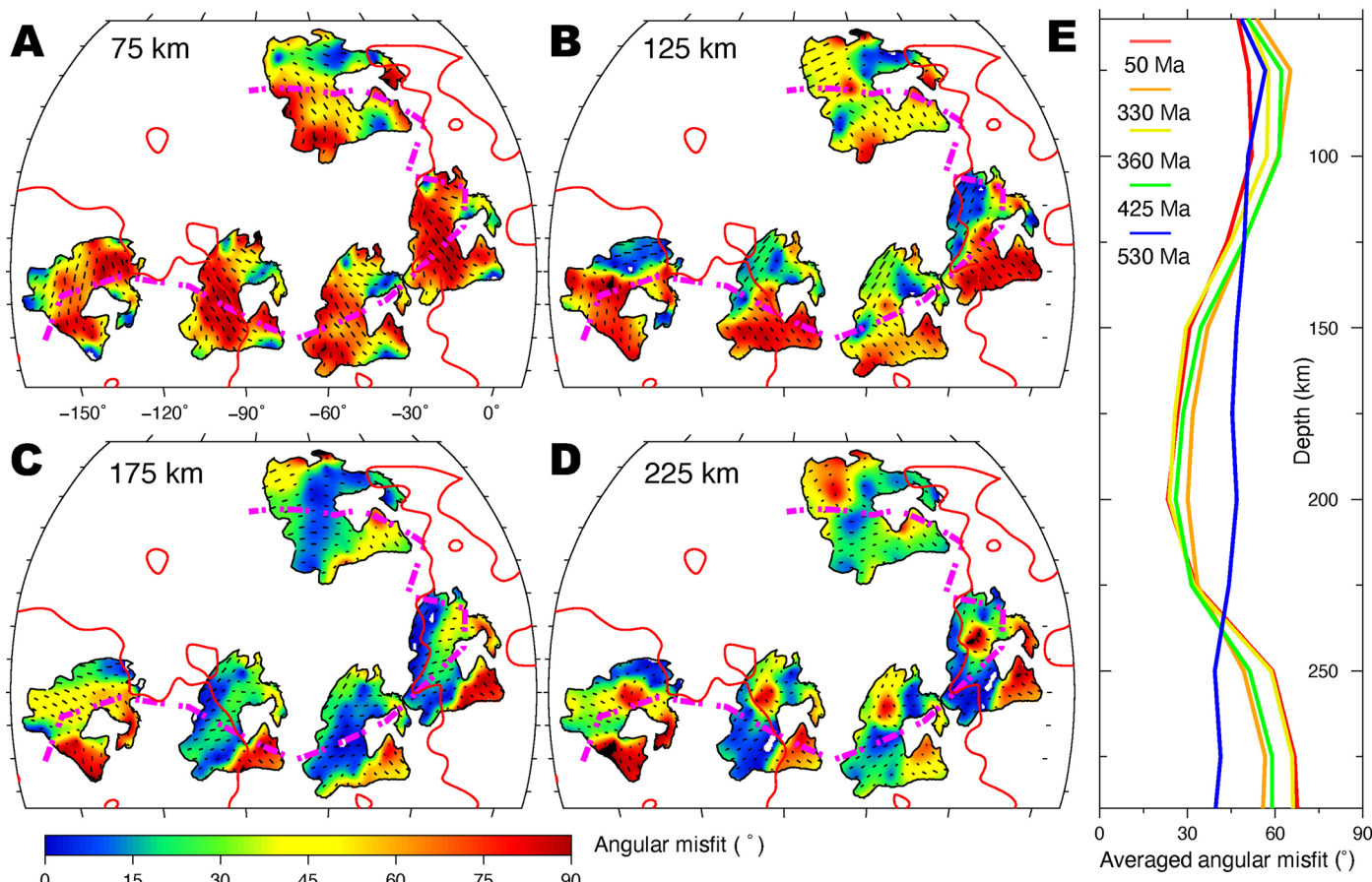
Availability). **(C)** Global LAB depth based on surface wave tomography⁶, with sites of Phanerozoic unroofing from Fig. 2. **(D)** Dynamic topography estimates based on S4ORTS²⁵, where seismic anomalies above the LAB (300 km for continents and 200 km for oceans) are assumed to be neutrally buoyant.



Extended Data Fig. 2 | Estimate of the pristine craton topography. (A) Observed craton topography plotted against crustal thickness. The error bars represent the corresponding standard deviations. (B) Craton topography after restoring erosion-removed crustal thickness to a nominal 41-km uniform thickness. (C) Pristine topography vs. present-day LAB depth for all cratons.

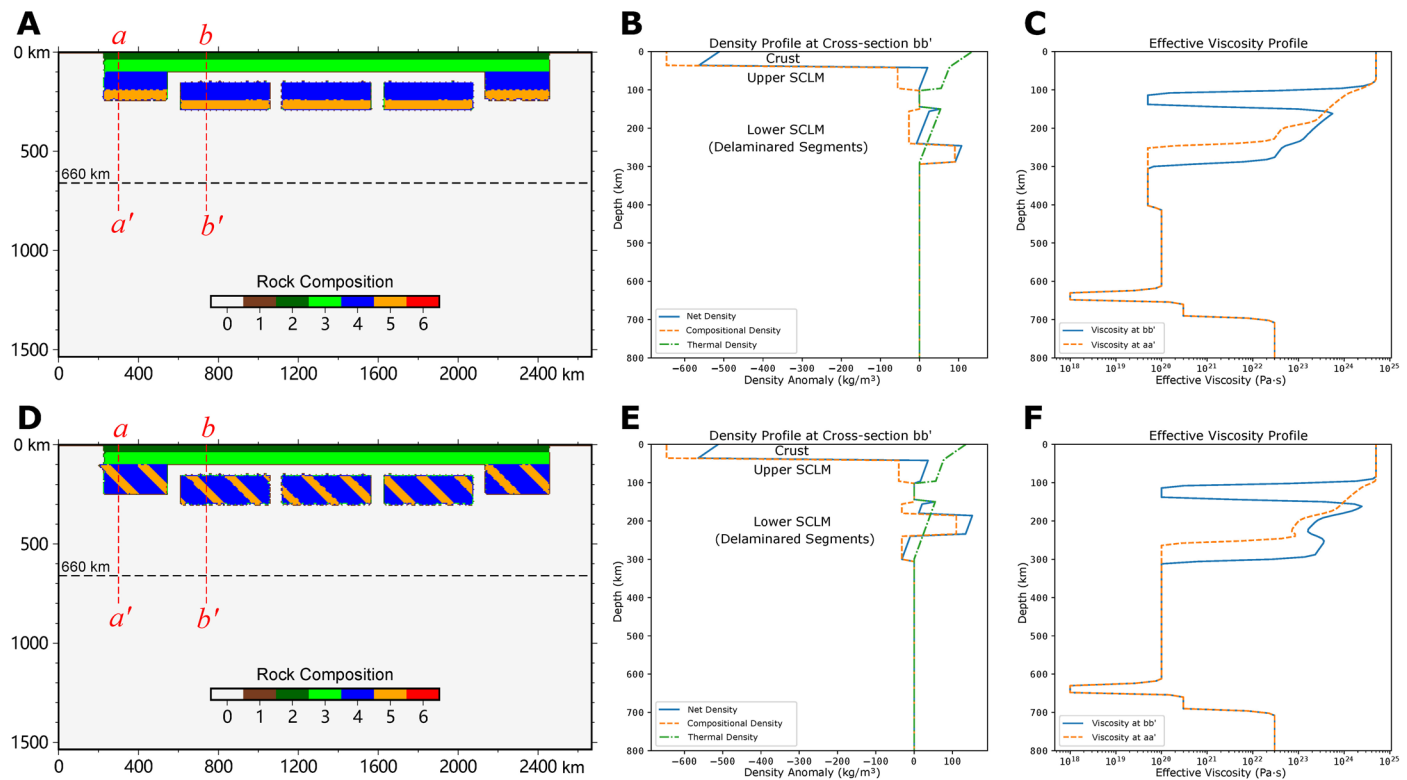


Extended Data Fig. 3 | Radial anisotropy from ref. 20. In the plot, $\xi = V_{SH}/V_{SV}$ with values > 1 represents faster horizontal than vertical polarization and vice versa. Magenta contours outline major cratons.



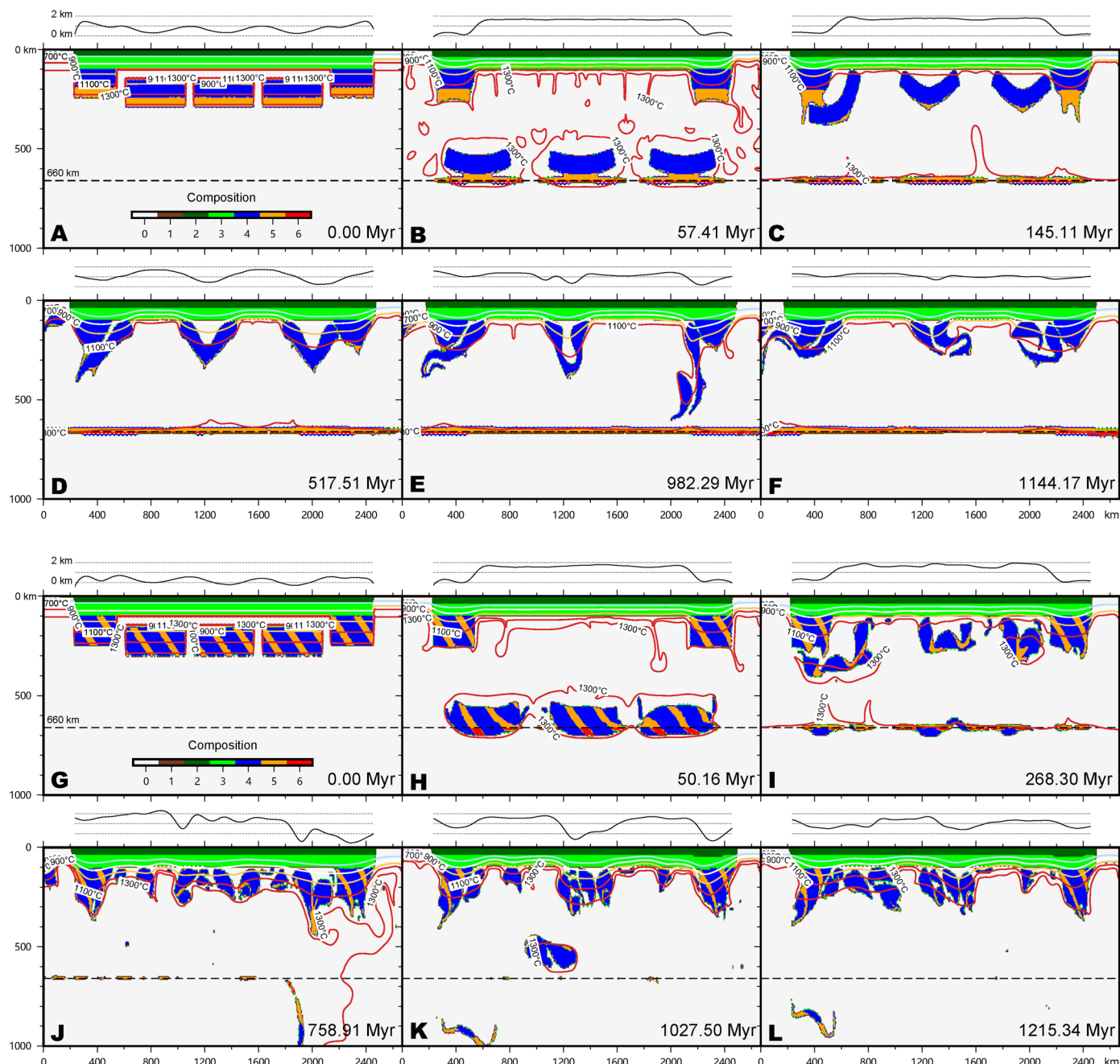
Extended Data Fig. 4 | Comparison of reconstructed North American anisotropy with Phanerozoic plate motion. (A–D) Fast axis of seismic anisotropy (black bars) over the North American craton from SL16³⁷ at depths ranging from 75 km to 225 km that are rotated back in time following past plate trajectory (the dash-dotted magenta line) and rotation²⁹. Each map corresponds to a different time interval (50 Myr for Paleozoic and 100 Myr for Mesozoic–

Cenozoic) whose middle points are shown in E. The background colors represent the angular misfit between the reconstructed fast orientation of anisotropy and averaged plate motion over the corresponding time interval. Red contours outline the two LLSPs. (E) Spatially averaged angular misfit with respect to depth and time.



Extended Data Fig. 5 | Initial model setup. (A) Compositional field of Model 4, where compositions of 0, 1, 2, 3, 4, 5, and 6, are ambient mantle, oceanic crust, continental crust, continental upper lithospheric mantle, compositionally buoyant lower SCLM, compositionally dense lower SCLM, and relatively

buoyant compositional 5 due to its delayed transformation at 660–750 km, respectively. (B–C) Density and viscosity profiles of the model initial condition. In C, the delaminated strong lower SCLM is shifted further down by ~50 km to demonstrate the decoupling zone above. (D–F) Same as (A–C), but for Model 5.



Extended Data Fig. 6 | Long-term evolution of the SCLM. (A-F) Model 4, with initial vertically stratified density profile in the lower SCLM. Background colors represent composition: 0 - ambient mantle, 1 - oceanic crust, 2 - cratonic crust, 3 - upper (< 100 km) SCLM, 4 - lower SCLM with 0.3% excess density, 5 - lower SCLM with 3% excess density, and 6 - bridgmanite. Overplotted are the evolving

geotherms. The top of each panel shows the corresponding surface topography. (G-L) Same as A-F but for Model 5 where the initial lower lithosphere has an imbricated density profile. More snapshots of the two geodynamic models are available in Supplementary Videos 3 & 4.

Extended Data Table 1 | Records^{55–64} of craton exhumation

<i>Tectonic events</i>	<i>Ref.</i>
Mesozoic & Cenozoic U.S.	Poag & Sevon, 1989 ⁵⁵
Neoproterozoic globe	Peters & Gains, 2012 ³⁰
South Atlantic margins	Guillocheau et al., 2012 ⁵⁶
Global craton basins	Allen & Armitage, 2012 ³¹
Phanerozoic Slave craton	Ault et al., 2013 ⁵⁷
Meso-Cenozoic eastern U.S.	Boettcher & Milliken, 1994 ⁵⁸
Mesozoic South Australia	Boone et al., 2016 ⁵⁹
Phanerozoic Sweden	Cederbom et al., 2000 ⁶⁰
Phanerozoic Brazil	Fonseca et al., 2021 ⁶¹
Meso-Cenozoic India	Sahu et al., 2013 ⁶²
Mesozoic South Africa	Stanley et al., 2013 ⁶³
Mesozoic South Africa	Wilman et al., 2017 ⁶⁴
Proterozoic Canadian Shield	McDannel & Zeitler, 2018 ⁶⁵

Extended Data Table 2 | Key parameters of geodynamic models

Model depth	1536km
Model width	2668km
Initial SCLM thickness	250 km
Vertical resolution	6km
Horizontal resolution	6km
Rayleigh number	5.08×10^8
Surface velocity boundary condition	Free slip
Surface temperature boundary condition	0°C
Bottom velocity boundary condition	Free slip
Bottom temperature boundary condition	1350°C
Ambient mantle temperature	1350°C
Clapeyron slope at 660km	-2MPa/K
Internal heating rate	11.8×10^{-12} W/kg